

Remote Cross-resonance Gate between Superconducting Fixed-frequency Qubits

Mari Ohfuchi and Shintaro Sato

Quantum Laboratory, Fujitsu Research, Fujitsu Limited, Atsugi 243-0197, Japan

E-mail: mari.ohfuti@fujitsu.com

17 December 2023

Abstract. High-fidelity quantum state transfer and remote entanglement between superconducting fixed-frequency qubits have not yet been realized. In this study, we propose an alternative remote cross-resonance gate. Considering multiple modes of a superconducting coaxial cable connecting qubits, we must find conditions under which the cross-resonance gate operates with a certain accuracy even in the presence of qubit frequency shifts due to manufacturing errors. For 0.25- and 0.5-m cables, remote cross-resonance gates with a concurrence of $> 99.9\%$ in entanglement generation are obtained even with ± 10 -MHz frequency shifts. For a 1-m cable with a narrow mode spacing, a concurrence of 99.5% is achieved by reducing the coupling between the qubits and cable. The optimized echoed raised-cosine pulse duration is 150–400 ns, which is similar to the operation time of cross-resonance gates between neighboring qubits on a chip. The dissipation through the cable modes does not considerably affect the obtained results. Such high-precision quantum interconnects pave the way not only for scaling up quantum computer systems but also for nonlocal connections on a chip. *Keywords:* superconducting fixed-frequency qubits, quantum interconnects, cross-resonance

1. Introduction

Superconducting quantum computers are a promising candidate for realizing practical large-scale quantum computation in the future [1, 2]. To scale up quantum computer systems, different levels of modularity and interconnects between them have been actively investigated [2–7]. One approach is to connect adjacent quantum chips with sufficiently short distances (~ 1 mm), which are the same as the distance between qubits on a single chip [4, 8–10], practically increasing the chip size and possibly allowing mapping of logical qubits encoded using surface codes [11–20]. Quantum chips separated by long distances in a refrigerator are connected through superconducting coaxial cables that pass microwave signals [5, 6, 21–29], millimeter-wave photonic links [30], or acoustic transmission lines as quantum phononic channels [31, 32]. For connecting qubits in different refrigerators or sending quantum information to the so-called quantum internet, quantum information stored in superconducting qubits must be frequency-converted into optical photons [7, 33–40]. However, it is very challenging to overcome large energy differences and achieve high conversion efficiencies. Herein, we focus on interconnects via 0.1–1-m superconducting coaxial cables inside a refrigerator [Fig. 1(a)]. Such medium-range quantum interconnects pave the way not only for scaling up quantum computer systems but also for nonlocal connections on a chip and thus non-two-dimensional (non-2D) quantum error-correcting codes [2, 11].

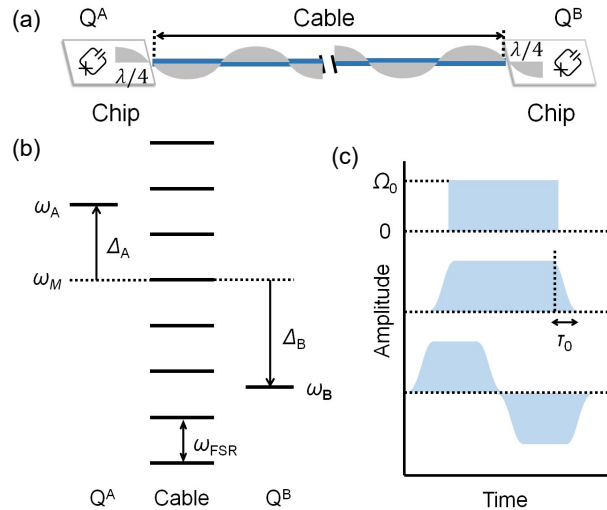


Figure 1. (a) Schematic of quantum interconnects via a coaxial cable and coplanar waveguides, where Q^A and Q^B are qubits and λ represents the wavelength. (b) Energy diagram: ω_A , ω_B , and ω_M are the frequencies of Q^A , Q^B , and the M th mode of the cable, respectively. The detunings of ω_A and ω_B measured from ω_M are denoted by Δ_A and Δ_B , respectively. The free spectral range ω_{FSR} corresponds to the equally spaced frequencies of the cable mode. (c) Schematic of cross-resonance pulse amplitudes: flat, raised-cosine, and echoed pulses from the top to bottom. The amplitude of the flat parts is Ω_0 , and the rise and fall times are τ_0 .

Quantum state transfer between two qubits through a superconducting coaxial cable

has been investigated using the pitch-and-catch scheme, wherein a photon emitted by a qubit at one end of the communication channel is received by another qubit at the opposite end [3,21–24]. In 2018, a fidelity of 80% was reported for quantum state transfer using a 0.9-m coaxial cable [22]. Half-quantum state transfer can generate a remote entangled state. A fidelity of 79% was reported for half-quantum state transfer [22]. Recent advances in fidelities have been achieved through a quantum state transfer scheme using the standing-wave modes of cables [5, 6, 25, 26]. A fidelity of 91% was reported for both quantum state transfer and remote entanglement through a 1-m cable [6]. Although the cable length was 0.25 m, the fidelity was increased to 99% by employing an aluminum low-loss coaxial cable and minimizing the dissipation at the junction between the cable and coplanar waveguides [Fig. 1(a)] [5]. However, the settings for these experiments are limited to the combination of frequency-tunable qubits [41–44] and tunable couplers [45] for matching the qubit frequency to the standing-wave mode of the cable. This can be because a small frequency detuning substantially reduces the transfer efficiency (Appendix A).

Fixed-frequency qubits have the advantages of long coherence times and noise immunity [46–54]. Low sensitivity to low-frequency charge and magnetic-flux fluctuations ensures qubit coherence. However, with current manufacturing processes of fixed-frequency qubits, slight frequency shifts are unavoidable [55, 56]. Even if qubits are fabricated at a frequency that matches the standing-wave mode of the cable, as mentioned above, a very small frequency detuning of 5 MHz [0.1% of a typical qubit frequency (approximately 5 GHz)] severely compromises the transfer efficiency. Thus, quantum state transfer using cable standing-wave modes is not applicable to fixed-frequency qubits. A two-qubit gate for fixed-frequency qubits is well known to use the cross-resonance effect [57–65]. Cross-resonance microwave signals enable conditional control between coupled qubits of different frequencies. Recent improvements in control pulses and coupling circuits have increased the fidelity of cross-resonance gates to 99.7%, with gate times of 100–400 ns [60, 62, 63]. In this study, we consider cross-resonance gates between two fixed-frequency qubits connected by a coaxial cable. More specifically, we explore the possibility of cross-resonance gates acting through multiple cable modes with an energy spacing similar to or narrower than qubit frequency detunings suitable for the cross-resonance effect.

The remainder of this paper is organized as follows. In Sec. II, we present the configuration of the transmission paths and reveal the fundamental properties of remote cross-resonance gates, such as concurrences as measures of entanglement generation and average gate fidelities. Section III focuses on the dissipative property of the transmission paths and its effect on the cross-resonance gates. In Sec. IV, we discuss leakage and single-qubit gate properties in remote cross-resonance gate settings. Finally, Sec. V presents the conclusions of the study and an outlook for future works.

2. Remote cross-resonance gate

We first configure the transmission paths and then present the fundamental properties of remote cross-resonance gates via these transmission paths. The qubit frequency dependence of the concurrence in entanglement generation is an important result of this work. We also introduce the average gate fidelity as a more general characteristic of two-qubit gates. In this section, we do not consider any dissipation to focus on the effect of multiple cable modes.

2.1. Transmission path

We consider a transmission path comprising a cable and coplanar waveguides as shown in Fig. 1(a). Target cable lengths are 0.25, 0.5, and 1 m. Let the frequency of the M th standing-wave mode of the cable be $\omega_M/(2\pi) = 5$ GHz [Fig. 1(b)]. Here, M is an odd number and is chosen such that the cable length is close to the target cable length. The cable and coplanar waveguide lengths are determined as follows:

$$\begin{aligned} l_{\text{Cable}} &= \frac{M-1}{2} \frac{v_{\text{Cable}}}{\omega_M/(2\pi)} = \frac{M-1}{2} \lambda_{\text{Cable}} \\ l_{\text{CPW}} &= \frac{1}{4} \frac{v_{\text{CPW}}}{\omega_M/(2\pi)} = \frac{1}{4} \lambda_{\text{CPW}}, \end{aligned} \quad (1)$$

where the microwave speeds in the cable and coplanar waveguide, $v_{\text{Cable}} = 2.472 \times 10^8$ m/s and $v_{\text{CPW}} = 1.157 \times 10^8$ m/s, respectively, were determined to reproduce the experimental results [5] and λ_{Cable} and λ_{CPW} are the microwave wavelengths in the cable and coplanar waveguide, respectively. The standing-wave mode spacing, namely free spectral range, is obtained as $\omega_{\text{FSR}} = \omega_M/M$. These characteristics of transmission paths are summarized in Table 1.

Table 1. Cable length (l_{Cable}), coplanar waveguide length (l_{CPW}), number of cable standing-wave mode for 5 GHz (M), and free spectral range (ω_{FSR}) for target cable lengths of 0.25, 0.5, and 1 m.

l_{Cable} (m)	l_{CPW} (mm)	M	$\omega_{\text{FSR}}/(2\pi)$ (GHz)
0.2966	5.8	13	0.3846
0.5438	5.8	23	0.2174
1.0832	5.8	43	0.1163

2.2. Remote cross-resonance Hamiltonian

Two fixed-frequency qubits Q^A and Q^B are connected to the transmission path [Fig. 1(a)]. The Hamiltonian for remote cross-resonance gates is given by

$$H_0 = \Delta_A \sigma_A^\dagger \sigma_A + \Delta_B \sigma_B^\dagger \sigma_B$$

$$\begin{aligned}
 & + \sum_{m=M_{\min}}^{M_{\max}} (m - M)\omega_{\text{FSR}}\sigma_m^\dagger\sigma_m \\
 & + \sum_{m=M_{\min}}^{M_{\max}} g_A\sqrt{\omega_m/\omega_M}(\sigma_A\sigma_m^\dagger + \sigma_A^\dagger\sigma_m) \\
 & + \sum_{m=M_{\min}}^{M_{\max}} (-1)^m g_B\sqrt{\omega_m/\omega_M}(\sigma_B\sigma_m^\dagger + \sigma_B^\dagger\sigma_m) \\
 H & = H_0 + \Omega(t)\cos(\tilde{\omega}_B t)\sigma_x^A, \tag{2}
 \end{aligned}$$

where σ_A , σ_B , and σ_m are annihilation operators for Q^A , Q^B , and the m th cable mode, Δ_A and Δ_B are the qubit frequency detunings measured from ω_M , and $\omega_m = m\omega_{\text{FSR}}$ is the m th cable mode frequency. The couplings between the qubits and the M th cable mode are g_A and g_B and proportional to the square root of the frequency in multimode coupling [6, 66].

The last term of the second equation in Eq. (2) represents a cross-resonance effect, and $\tilde{\omega}_B$ is the dressed qubit frequency of Q^B that is by solving an eigenvalue problem for H_0 . The cross-resonance pulse envelope $\Omega(t)$ is schematically presented in Fig. 1(c). We consider three pulse envelopes: flat pulse envelope, raised-cosine pulse envelope to reduce spectral leakage in the frequency domain [67, 68], and echoed pulse envelope to equalize the difference in pulse duration due to the initial state [59, 60]. We fix the amplitude of the flat parts to $\Omega_0/(2\pi) = 0.1$ GHz and the rise and fall times for the raised-cosine and echoed pulses to $\tau_0 = 100 \times 2\pi/\tilde{\omega}_B \sim 20$ ns because the cross-resonance effect can be adjusted by the total pulse duration τ .

We write the qubit states as $|\Phi_i\rangle = c_{i,|00\rangle}|00\rangle + c_{i,|01\rangle}|01\rangle + c_{i,|10\rangle}|10\rangle + c_{i,|11\rangle}|11\rangle$, where each ket represents the eigenstate of H_0 in order of $Q^A Q^B$. The ideal cross-resonance gate is expressed as

$$[ZX]^{1/2} = \frac{1}{\sqrt{2}} \begin{pmatrix} 1 & -i & 0 & 0 \\ -i & 1 & 0 & 0 \\ 0 & 0 & 1 & i \\ 0 & 0 & i & 1 \end{pmatrix}, \tag{3}$$

which is combined with two single-qubit gates to form a CNOT gate (i.e., $\text{CNOT} = [ZI]^{-1/2}[ZX]^{1/2}[IX]^{-1/2}$). The CNOT gate results in remote state transfer for the initial state of $|\Phi_1^I\rangle = |10\rangle$ and forms a Bell state as a maximum entangled state for $|\Phi_+^I\rangle = (|00\rangle + |10\rangle)/\sqrt{2}$.

2.3. Time evolution simulation

Herein, we present details of time evolution simulations using the case of a 0.25-m coaxial cable. In the Hamiltonian of Eq. (2), we set $M = 13$ and $\omega_{\text{FSR}}/(2\pi) = 0.3846$ GHz from Table 1. Let $\Delta_A = 0.7\omega_{\text{FSR}}$ and $\Delta_B = -0.3\omega_{\text{FSR}}$, then $\omega_A > \omega_M$ and $\omega_B < \omega_M$ as shown in Fig. 1(b). This is written as $\delta_A = |\Delta_A|/\omega_{\text{FSR}} = 0.7$ and $\delta_B = |\Delta_B|/\omega_{\text{FSR}} = 0.3$ and results in a qubit frequency detuning of $\Delta/(2\pi) = (\omega_A - \omega_B)/(2\pi) = 0.3846$ GHz. Two cable modes above ω_A and two below ω_B yield the upper and lower cable mode limits

$M_{\max} = 15$ and $M_{\min} = 11$, respectively. The coupling between the qubits and cable modes is chosen as $g_A/(2\pi) = g_B/(2\pi) = g/(2\pi) = 0.03$ GHz. We numerically simulate time evolution using the QuTip framework [69, 70]. The results with a cross-resonance pulse are presented in Figure 2.

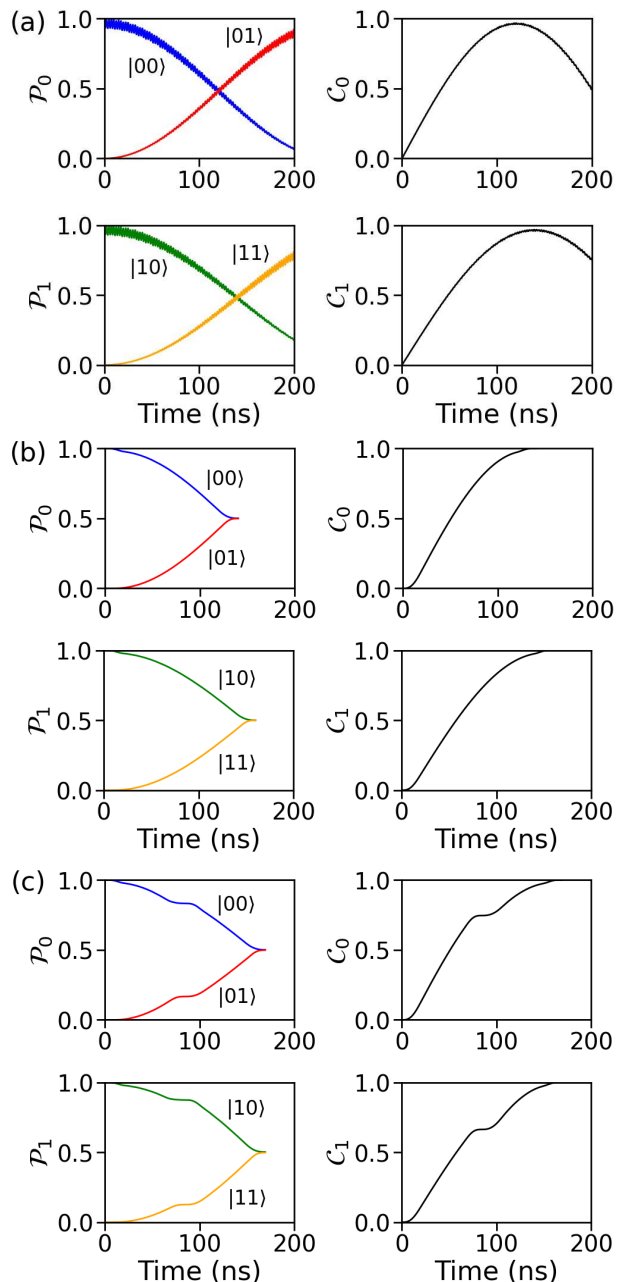


Figure 2. Time evolution with (a) flat, (b) raised-cosine, and (c) echoed cross-resonance pulses for a 0.25-m coaxial cable: occupation probability of the qubit states \mathcal{P} and concurrence \mathcal{C} . For each figure, the upper and lower panels show the results with the initial qubit states of $|\Phi_0^I\rangle = |00\rangle$ and $|\Phi_1^I\rangle = |10\rangle$, respectively. Other parameters are $g/(2\pi) = 0.03$ GHz, $\delta_A = 0.7$, and $\delta_B = 0.3$ [$\Delta/(2\pi) = 0.3846$ GHz].

We first consider the initial qubit states of $|\Phi_0^I\rangle = |00\rangle$ and $|\Phi_1^I\rangle = |10\rangle$. When

$[ZX]^{1/2}$ is applied, $|\Phi_0^I\rangle$ and $|\Phi_1^I\rangle$ become $|\Phi_0^F\rangle = (|00\rangle - i|01\rangle)/\sqrt{2}$ and $|\Phi_1^F\rangle = (|10\rangle + i|11\rangle)/\sqrt{2}$, respectively. Figure 2(a) presents the results with a flat cross-resonance pulse applied continuously for 200 ns. The amplitude of the cross-resonance pulse is set to $\Omega_0/(2\pi) = 0.1$ GHz, as described above. The occupation probability of the qubit state is given as $\mathcal{P}_{i,k} = |c_{i,k}|^2$ for each k state. The \mathcal{P}_0 for $|\Phi_0^I\rangle$ and \mathcal{P}_1 for $|\Phi_1^I\rangle$ are shown in the left panels. With increasing time, $\mathcal{P}_{0,|00\rangle}$ decreases from 1, $\mathcal{P}_{0,|01\rangle}$ increases from 0, and $\mathcal{P}_{0,|00\rangle}$ and $\mathcal{P}_{0,|01\rangle}$ intersect at approximately $\mathcal{P}_0 = 0.5$ and 120 ns. Similarly, $\mathcal{P}_{1,|10\rangle}$ and $\mathcal{P}_{1,|11\rangle}$ intersect at approximately $\mathcal{P}_1 = 0.5$ and 140 ns. We define the concurrences

$$\begin{aligned}
 \mathcal{C}_0 &= 2|c_{0,|00\rangle}||c_{0,|01\rangle}| \\
 \mathcal{C}_1 &= 2|c_{1,|10\rangle}||c_{1,|11\rangle}|
 \end{aligned} \tag{4}$$

so that they become 1 when $|\Phi_i\rangle = |\Phi_i^F\rangle$. The right panels of Fig. 2(a) show \mathcal{C}_0 and \mathcal{C}_1 . The concurrence takes the maximum values of $\mathcal{C}_0 = 96.82\%$ at 120.1 ns and $\mathcal{C}_1 = 96.86\%$ at 139.4 ns, which are near the time of the intersection of each \mathcal{P} . These results show that the cross-resonance pulses with parameters currently under consideration can fundamentally act as a $[ZX]^{1/2}$ gate with a pulse duration similar to those of cross-resonance gates between neighboring qubits on a chip [60, 63].

To reduce spectral leakage in the frequency domain, a raised-cosine pulse is employed. We fix the rise and fall time to $\tau_0 = 100 \times 2\pi/\tilde{\omega}_B = 20.5$ ns and find the pulse duration τ when \mathcal{C}_0 and \mathcal{C}_1 take their maximum values. We obtain the maximum value of $\mathcal{C}_0 = \mathcal{C}_1 = 100.00\%$ at $\tau = 140.4$ ns for $|\Phi_0^I\rangle$ and $\tau = 159.9$ ns for $|\Phi_1^I\rangle$. The time evolution during the raised-cosine pulse for each initial state is depicted in Fig. 2(b).

Further, to equalize the difference in τ due to the initial state, we adopt an echoed cross-resonance pulse. To isolate the precision of remote cross-resonance gates, two single-qubit π rotations for Q^A are analytically performed during the process. The rise and fall times are again fixed to $\tau_0 = 100 \times 2\pi/\tilde{\omega}_B = 20.5$ ns. We find τ when \mathcal{C}_0 and \mathcal{C}_1 take their maximum values. We obtain $\tau = 169.3$ ns and the maximum $\mathcal{C} = 100.00\%$ for both $|\Phi_0\rangle$ and $|\Phi_1\rangle$. Figure 2(c) depicts the time evolution during the echoed cross-resonance pulse for each initial state $|\Phi_0\rangle$ and $|\Phi_1\rangle$.

We have examined the case where the cross-resonance signal is input from a higher-frequency qubit to a lower-frequency qubit. Here, conversely, the qubit frequency detunings are set to $\Delta_A = -0.3\omega_{\text{FSR}}$ and $\Delta_B = 0.7\omega_{\text{FSR}}$. We confirm almost the same results with an echoed cross-resonance pulse, $\mathcal{C}_0 = 99.99\%$, $\mathcal{C}_1 = 100.00\%$, and $\tau = 160.3$ ns, as those described above. Thus, we continue our study by focusing on a cross-resonance signal from a higher-frequency qubit.

One important consideration for remote cross-resonance gates is the degree of entanglement generation [5, 6, 22, 25]. We simulate time evolution with the echoed remote cross-resonance pulse determined above for the initial qubit state of $|\Phi_+^I\rangle = (|00\rangle + |10\rangle)/\sqrt{2}$. When $[ZX]^{1/2}$ is applied to $|\Phi_+^I\rangle$, we obtain $|\Phi_+^F\rangle = (|00\rangle - i|01\rangle + |10\rangle + i|11\rangle)/2$, which is an entangled state, unlike $|\Phi_0^F\rangle$ and $|\Phi_1^F\rangle$. With a qubit state

$|\Phi_+\rangle$, the concurrence as a measure of entanglement is defined by

$$\mathcal{C}_+ = 16|c_{+,|00}\rangle||c_{+,|01}\rangle||c_{+,|10}\rangle||c_{+,|11}\rangle| \quad (5)$$

so that this becomes 1 when $|\Phi_+\rangle = |\Phi_+^F\rangle$. We obtain the concurrence $\mathcal{C}_+ = 100.00\%$. Thus, we examine the qubit frequency dependence of \mathcal{C}_+ in the next section.

2.4. Qubit frequency dependence

Let us consider the range of qubit frequencies in which the remote cross-resonance gate operates efficiently. We examine the maximum value of \mathcal{C}_+ with an echoed cross-resonance pulse for each δ_A and δ_B in the ranges $\delta_i \neq 0, 1, 2 \dots$, where $\delta_i = |\Delta_i|/\omega_{\text{FSR}}$, $i = A$ and B , because $\delta_i = 0, 1, 2, \dots$ do not well define the qubit state owing to the same energy levels of the qubit and cable mode [Fig. 1(b)].

2.4.1. 0.25-m coaxial cable Figure 3 summarizes the maximum \mathcal{C}_+ and echoed pulse duration τ in the range $0.1 \leq \delta_A \leq 0.9$ and $0.1 \leq \delta_B \leq 0.9$ for a 0.25-m coaxial cable with $g/(2\pi) = 0.03$ GHz. We can find 3×3 cells with $\mathcal{C}_+ > 99.9\%$ in the top-right part ($0.1 \leq \delta_A \leq 0.3$ and $0.6 \leq \delta_B \leq 0.8$) with $\tau \sim 160$ ns. The frequency detuning of $\delta_i = 0.1$ corresponds to 38.5 MHz. This means that if we aim for the frequencies of $\delta_A = 0.2$ and $\delta_B = 0.7$ to fabricate the qubits, even with ± 38 -MHz frequency error due to manufacturing, obtaining $\mathcal{C}_+ > 99.9\%$ is possible by calibrating the signal frequency and pulse duration. A standard deviation of the frequency distribution of $\sigma_f = 14$ MHz has already been achieved with the current technology [55, 56].

	0.1	0.2	0.3	0.4	0.5	0.6	0.7	0.8	0.9
0.1		0.9809 57.2	0.9977 97.2	0.9129 115.2	0.9755 139.4	0.9993 153.9	0.9999 157.2	0.9991 147.3	0.9993 126.9
0.2	0.9909 46.7	0.9966 83.5	0.9970 107.0	0.9982 129.7	0.9858 149.4	1.0000 161.9	1.0000 161.8	1.0000 149.0	0.9944 125.2
0.3	0.9995 137.5	0.9992 92.0	0.9525 116.4	0.9998 142.5	0.9914 161.9	1.0000 173.2	1.0000 171.1	0.9999 154.9	0.9999 129.0
0.4	0.9986 58.3	0.9995 101.4	0.9994 128.3	0.9916 156.1	0.9928 175.6	1.0000 185.8	1.0000 181.7	0.9886 162.6	1.0000 134.6
0.5	0.9994 84.1	0.9771 109.9	0.9999 140.6	1.0000 169.3	0.9839 193.1	0.9999 200.0	0.9999 193.9	0.9999 172.8	1.0000 141.0
0.6	0.9986 91.4	0.9997 120.5	0.9998 153.7	1.0000 184.6	0.9980 206.8	0.9572 220.6	0.9837 206.2	1.0000 183.5	1.0000 148.7
0.7	0.9892 99.1	0.9999 132.3	1.0000 169.3	1.0000 202.8	0.9990 226.8	0.9998 235.7	0.8552 225.6	0.9998 197.5	0.9999 158.6
0.8	0.9997 111.2	1.0000 150.2	1.0000 193.1	0.9999 231.7	0.9991 258.4	0.9819 264.6	0.9986 253.9	0.6663 191.1	0.9948 174.0
0.9	0.9987 137.5	0.9987 191.3	0.9990 251.7	0.9988 302.3	0.9985 336.7	0.9996 345.1	0.9999 322.0	0.9995 273.7	0.5669 171.0

Figure 3. Time evolution simulation results of an echoed cross-resonance pulse with the initial qubit state of $|\Phi_+^I\rangle = (|00\rangle + |10\rangle)/\sqrt{2}$ for a 0.25-m coaxial cable with $g/(2\pi) = 0.03$ GHz. The numbers in the titles of rows and columns are the qubit frequency detunings $\delta_A = |\Delta_A|/\omega_{\text{FSR}}$ and $\delta_B = |\Delta_B|/\omega_{\text{FSR}}$, respectively. In each cell, the top figure is the concurrence \mathcal{C}_+ and the bottom figure is the duration τ in ns. The cells are colored according to their \mathcal{C}_+ values (blue: $>99.9\%$, green: $>99\%$, orange: $>90\%$, and white: $\leq 90\%$).

We can find other 3×3 cells with $\mathcal{C}_+ > 99.9\%$ in the bottom left ($0.6 \leq \delta_A \leq 0.8$ and $0.2 \leq \delta_B \leq 0.4$). The results for the center of this area, $\delta_A = 0.7$ and $\delta_B = 0.3$,

have been shown in the previous section and are summarized in Table 2 as an example. The maximum \mathcal{C}_+ in the diagonal cells is smaller than the others. We find that this degradation is due to the closeness of the energy levels of the qubit $|11\rangle$ state and the cable state comprising two cable modes $M \pm k$. This is a notable feature in remote cross-resonance gates through cables with multimode coupling.

A smaller coupling of $g/(2\pi) = 0.02$ GHz is also examined (Appendix B, Fig. B1(a)). Despite the increase in τ (~ 300 ns), the range with $\mathcal{C}_+ > 99.9\%$ does not expand. Although some cells with $\mathcal{C}_+ \leq 99\%$ change to $\mathcal{C}_+ > 99\%$ and the cell where the qubit state is not defined disappears, it is not beneficial to make the coupling smaller in this case, where high \mathcal{C}_+ values are already obtained over a wide range.

2.4.2. 0.5-m coaxial cable The free spectral range for a 0.5-m coaxial cable is a small value of $\omega_{\text{FSR}}/(2\pi) = 0.2174$ GHz (Table 1). We consider the range $1.1 \leq \delta_A \leq 1.9$ and $0.1 \leq \delta_B \leq 0.9$ to include the region $\Delta/(2\pi) \sim 0.4$ GHz where high \mathcal{C}_+ is obtained for a 0.25-m coaxial cable. The results for $g/(2\pi) = 0.03$ GHz are shown in Fig. 4(a). As in the case of a 0.25-m coaxial cable, we can find two 2×2 cells with $\mathcal{C}_+ > 99.9\%$ [$(1.2 \leq \delta_A \leq 1.3$ and $0.7 \leq \delta_B \leq 0.8)$ and $(1.4 \leq \delta_A \leq 1.5$ and $0.8 \leq \delta_B \leq 0.9)$] for $\tau \sim 150$ ns. The frequency detuning of $\delta_i = 0.1$ corresponds to 21.7 MHz. This means that if we aim for the frequencies of the center of the areas to fabricate the qubits, obtaining $\mathcal{C}_+ > 99.9\%$ is possible even with ± 10 MHz frequency error owing to manufacturing. The center of the area $\delta_A = 1.25$ and $\delta_B = 0.75$ gives $\mathcal{C}_+ = 99.98\%$, which is included in Table 2, and $\delta_A = 1.45$ and $\delta_B = 0.85$ also gives $\mathcal{C}_+ = 99.98\%$. We find some 2×2 cells with $\mathcal{C}_+ > 99.9\%$ in the range $0.1 \leq \delta_A \leq 0.9$ and $1.1 \leq \delta_B \leq 1.9$ (Appendix B, Fig. B1(b)).

The range $0.1 \leq \delta_A \leq 0.9$ and $0.1 \leq \delta_B \leq 0.9$, where Δ exhibits small values, are also examined. As shown in Fig. 4(b), reducing the coupling to $g/(2\pi) = 0.02$ GHz leads to 2×2 cells with $\mathcal{C}_+ > 99.9\%$ and the average values of $\tau \sim 150$ ns and $\Delta/(2\pi) \sim 0.22$ GHz. The center of the area $\delta_A = 0.35$ and $\delta_B = 0.65$ gives $\mathcal{C}_+ = 99.98\%$ for $\tau = 147.3$ ns, which is also included in Table 2.

2.4.3. 1-m coaxial cable The free spectral range for a 1-m coaxial cable is a further small value of $\omega_{\text{FSR}}/(2\pi) = 0.1163$ GHz (Table 1). The range $2.1 \leq \delta_A \leq 2.9$ and $1.1 \leq \delta_B \leq 1.9$ includes the region $\Delta/(2\pi) \sim 0.4$ GHz where high \mathcal{C}_+ is obtained for a 0.25-m coaxial cable. However, the coupling $g/(2\pi) = 0.03$ GHz does not provide well-defined qubit states over the entire range. The results for the range with $g/(2\pi) = 0.02$ GHz are presented in Fig. 5(a). We find 2×2 cells with $\mathcal{C}_+ > 99\%$ in the bottom-left part ($2.5 \leq \delta_A \leq 2.6$ and $1.2 \leq \delta_B \leq 1.3$). The center of the area $\delta_A = 2.55$ and $\delta_B = 1.25$ gives $\mathcal{C}_+ = 99.28\%$, and the results are summarized in Table 2. We cannot obtain an area with $\mathcal{C}_+ > 99.9\%$ as in the cases of 0.25- and 0.5-m cables. It is found that the occupation probability of the cable states with energies corresponding to $\sim 2\tilde{\omega}_B$ or $\sim 3\tilde{\omega}_B$ gradually increases during the cross-resonance pulse. This can be the most important characteristic with regard to remote cross-resonance gates through

	0.1	0.2	0.3	0.4	0.5	0.6	0.7	0.8	0.9
(a) 1.1				0.9830 171.2	0.9777 186.2	0.9962 188.1			
1.2			0.4254 112.9	0.9513 154.5	0.9732 169.4	0.9989 171.3	0.9998 162.4	0.9996 147.3	
1.3	0.9982 102.5	0.9925 121.8	0.5941 150.3	0.7166 179.0	0.9554 165.3	0.9984 165.9	0.9997 157.5	0.9999 143.1	
1.4	0.9960 103.7	0.9795 121.0	0.9838 137.7	0.6624 178.5	0.8124 173.9	0.9890 168.0	0.9986 157.9	0.9998 143.6	0.9998 127.4
1.5	0.9937 106.1	0.9972 124.3	0.9989 143.0	0.9735 158.6	0.6898 188.6	0.9273 180.7	0.9912 162.4	0.9993 146.4	0.9997 129.9
1.6	0.9938 110.6	0.9989 129.5	0.9997 149.5	0.9959 167.1	0.9701 178.8	0.5914 164.3	0.9430 175.6	0.9904 151.4	0.9981 134.4
1.7	0.9992 117.4	0.9998 138.0	0.9994 159.6	0.9995 177.7	0.9936 188.6	0.9667 188.5	0.5348 144.3	0.9169 168.0	
1.8		0.9994 152.2	0.9983 176.3	0.9995 196.9	0.9969 207.5	0.9898 208.2	0.9802 192.9	0.5100 137.8	
1.9			0.9969 208.8	0.9978 229.1	0.9957 245.1	0.9971 248.1			

	0.1	0.2	0.3	0.4	0.5	0.6	0.7	0.8	0.9
(b) 0.1		0.9084 54.2	0.8769 82.4	0.9324 111.2	0.9490 115.7	0.9750 122.0	0.9835 124.1	0.9930 122.1	0.9536 107.2
0.2	0.9024 47.7	0.9546 60.4	0.8691 92.5	0.9712 113.6	0.9697 126.8	0.9975 133.9	0.9990 133.6	0.9957 124.6	0.9787 107.6
0.3	0.9153 50.5	0.9454 84.9	0.9379 104.7	0.9609 120.6	0.9734 135.4	0.9993 142.9	0.9996 140.6	0.9840 129.2	0.9935 111.4
0.4	0.9402 56.4	0.9275 90.5	0.9967 112.0	0.9990 131.6	0.9028 140.7	0.9997 152.4	0.9992 148.9	0.9820 134.5	0.9961 115.9
0.5	0.9735 80.6	0.9598 99.0	0.9981 121.3	0.9993 141.7	0.9909 155.8	0.8596 154.0	0.9833 158.3	0.9987 142.4	0.9979 121.7
0.6	0.9677 85.0	0.9979 107.5	0.9975 131.8	0.9992 154.0	0.9904 168.9	0.9980 175.8	0.8264 160.4	0.9979 151.1	0.9982 128.0
0.7	0.9741 92.6	0.9940 118.8	0.9968 146.9	0.9975 171.1	0.9938 189.0	0.9896 193.8	0.9944 188.9	0.8230 157.7	0.9969 137.9
0.8	0.9763 107.9	0.9962 143.1	0.9917 179.7	0.9843 200.4	0.9962 224.9	0.9734 225.1	0.9890 215.7	0.8895 204.1	0.7881 143.8
0.9	0.9752 157.1	0.9982 207.3	0.8885 219.5	0.9240 265.2	0.9747 308.8	0.9804 307.6	0.9924 302.3	0.9834 257.1	0.5053 155.8

Figure 4. Time evolution simulation results of an echoed cross-resonance pulse with the initial qubit state of $|\Phi_+\rangle = (|00\rangle + |10\rangle)/\sqrt{2}$ for a 0.5-m coaxial cable: (a) $g/(2\pi) = 0.03$ GHz and (b) $g/(2\pi) = 0.02$ GHz. Other explanations are the same as those in Fig. 3

cables with multimode coupling. However, if we aim for the frequencies of $\delta_A = 2.55$ and $\delta_B = 1.25$ to fabricate the qubits, even in case of manufacturing errors of ± 5 MHz, it is possible to obtain $\mathcal{C}_+ > 99\%$, which is in sharp contrast to quantum state transfer, where a detuning of 5 MHz substantially reduces the efficiency, as mentioned earlier. The frequency shift of 5 MHz corresponds to 0.1% of the qubit frequency ~ 5 GHz and matches the standard deviation of the frequency distribution that is required to achieve a 1000-qubit computer [55, 56]. We also find two 2×2 cells with $\mathcal{C}_+ > 99\%$ in the range $1.1 \leq \delta_A \leq 1.9$ and $2.1 \leq \delta_B \leq 2.9$ (Appendix B, Fig. B1(c)).

Unlike in the case of a 0.25-m coaxial cable, it is very beneficial to reduce the coupling to $g/(2\pi) = 0.01$ GHz. Although τ increases, we can find much wider areas with $\mathcal{C}_+ > 99\%$ as shown in Fig. 5(b). For example, there are 3×3 cells ($2.4 \leq \delta_A \leq 2.6$ and $1.1 \leq \delta_B \leq 1.3$) with $\mathcal{C}_+ > 99.5\%$ for $\tau \sim 400$ ns. This corresponds to allowing manufacturing errors of ± 11 MHz for $\mathcal{C}_+ > 99.5\%$. The center of the area $\delta_A = 2.5$ and $\delta_B = 1.2$ gives $\mathcal{C}_+ = 99.64\%$, which is included in Table 2. The range $1.1 \leq \delta_A \leq 1.9$ and $1.1 \leq \delta_B \leq 1.9$ for $g/(2\pi) = 0.01$ GHz are also examined, and the results are presented in Fig. 5(c). Numerous 2×2 cells with $\mathcal{C}_+ > 99\%$ are obtained. Among them, the area centered on $\delta_A = 1.55$ and $\delta_B = 1.35$ leads to $\mathcal{C}_+ > 99.5\%$. The results on the center of $\mathcal{C}_+ = 99.84\%$ and $\tau = 400.3$ ns are also included in Table 2.

To summarize the results thus far, as shown in Table 2, there are qubit frequencies of $\mathcal{C}_+ > 99.9\%$ for 0.25- and 0.5-m cables even with manufacturing errors of ± 38 MHz

	1.1	1.2	1.3	1.4	1.5	1.6	1.7	1.8	1.9
(a) 2.1									
2.2			0.4273 147.5	0.9502 239.3	0.9489 236.8	0.9869 220.2			
2.3		0.9932 181.9	0.8370 223.5	0.4518 158.1	0.9480 227.3	0.9727 221.9	0.9948 205.2		
2.4		0.9824 182.7	0.9800 197.9	0.8402 240.5	0.4758 165.9	0.9870 225.6	0.9772 206.5	0.9947 189.7	
2.5		0.9945 186.0	0.9944 207.8	0.9639 219.0	0.8647 255.5	0.5019 170.4	0.9797 218.6	0.9872 191.8	
2.6		0.9924 196.8	0.9935 219.0	0.9930 229.8	0.9565 231.9	0.7558 265.5	0.6854 585.7		
2.7		0.9891 212.8	0.9961 237.6	0.9893 249.6	0.9840 262.5	0.9724 245.6	0.5167 232.7		
2.8				0.9844 789.0	0.9929 303.2				
2.9									

	1.1	1.2	1.3	1.4	1.5	1.6	1.7	1.8	1.9
(b) 2.1	0.9609 298.8	0.4637 262.7	0.9844 500.2	0.9852 568.7	0.9855 635.9	0.9811 639.4	0.9814 515.1	0.9789 446.5	0.9852 319.4
2.2	0.9793 286.9	0.9437 400.3	0.4856 344.6	0.9809 552.6	0.9940 602.3	0.9907 604.1	0.9943 510.1	0.9933 410.6	0.9946 311.1
2.3	0.9912 281.5	0.9952 370.6	0.9877 481.2	0.4845 384.2	0.9956 580.4	0.9978 578.4	0.9969 505.9	0.9964 416.5	0.9959 311.1
2.4	0.9951 282.8	0.9967 378.0	0.9972 486.2	0.9894 573.3	0.5152 437.3	0.9982 583.3	0.9986 518.4	0.9968 421.5	0.9985 317.8
2.5	0.9965 289.8	0.9964 386.7	0.9989 496.5	0.9968 577.8	0.9944 624.7	0.4967 667.3	0.9976 535.9	0.9964 431.9	0.9982 322.8
2.6	0.9968 302.1	0.9970 411.8	0.9965 515.9	0.9979 608.0	0.9969 652.1	0.9838 613.3	0.6717 556.3	0.9943 449.0	0.9945 335.3
2.7	0.9951 319.4	0.9920 441.5	0.9869 527.4	0.9981 644.4	0.9958 702.7	0.9915 642.3	0.9932 575.5	0.7071 499.1	0.9802 366.3
2.8	0.9751 389.6	0.9883 490.9	0.9961 654.9	0.9948 738.7	0.9958 819.1	0.9866 735.8	0.9789 647.9	0.9386 557.5	0.6799 386.3
2.9	0.7270 367.0	0.8544 553.9	0.9167 747.4	0.9035 845.4	0.8595 846.1	0.3614 465.3	0.4406 466.8	0.6137 459.5	0.4563 452.0

	1.1	1.2	1.3	1.4	1.5	1.6	1.7	1.8	1.9
(c) 1.1	0.9549 215.8	0.8526 277.6	0.8889 396.6	0.9357 347.4	0.9832 408.3	0.9878 412.1	0.9740 358.1	0.9608 300.0	0.9755 239.2
1.2	0.9687 194.8	0.9767 274.7	0.8886 328.5	0.9856 374.3	0.9871 421.6	0.9907 425.0	0.9923 381.0	0.9802 300.0	0.9922 242.9
1.3	0.9910 204.3	0.9897 272.6	0.9918 341.7	0.8926 423.9	0.9594 425.7	0.9920 426.3	0.9937 389.7	0.9978 319.6	0.9946 244.2
1.4	0.9957 210.4	0.9916 279.6	0.9965 347.1	0.9900 400.8	0.8166 461.0	0.9819 435.8	0.9954 386.0	0.9972 322.2	0.9942 247.9
1.5	0.9949 217.8	0.9949 292.4	0.9963 360.3	0.9955 412.8	0.9890 448.9	0.6615 399.3	0.9838 405.6	0.9947 333.8	0.9922 256.3
1.6	0.9936 226.1	0.9892 308.0	0.9977 387.5	0.9976 440.5	0.9964 482.1	0.9836 477.4	0.5850 332.3	0.9762 345.1	0.9903 268.0
1.7	0.9780 264.3	0.9860 348.0	0.9921 417.2	0.9946 483.1	0.9908 543.5	0.9783 483.2	0.9924 467.2	0.5494 281.3	0.9725 306.1
1.8	0.9401 329.2	0.9915 428.3	0.2677 961.1	0.9892 605.1	0.9701 604.4	0.9767 599.5	0.9543 512.2	0.1958 841.7	0.5412 246.3
1.9	0.4839 267.2	0.4972 361.6	0.5038 459.3	0.3943 460.3	0.3595 461.8	0.3860 462.8	0.1676 271.9	0.2624 273.3	0.1628 177.7

Figure 5. Time evolution simulation results of an echoed cross-resonance pulse with the initial qubit state of $|\Phi_+^I\rangle = (|00\rangle + |10\rangle)/\sqrt{2}$ for a 1-m coaxial cable: (a) $g/(2\pi) = 0.02$ GHz and (b) (c) $g/(2\pi) = 0.01$ GHz. Other explanations are the same as those in Fig. 3.

and ± 10 MHz, respectively, and $\mathcal{C}_+ > 99\%$ for a 1-m cable even with ± 5 -MHz. In the case of a 1-m cable, by reducing the coupling between the qubits and cable, although τ increases, the lower limit of \mathcal{C}_+ and allowed manufacturing error can be 99.5% and ± 11 MHz. These are in contrast to quantum state transfer, where a small detuning of 5 MHz substantially reduces the efficiency (Appendix A).

2.5. Average gate fidelity

We have focused on the concurrence as a measure of remote entanglement generation. Herein, we investigate the average gate fidelity as a more general characteristic of two-qubit gates. The average gate fidelity is also important because it is obtained in randomized benchmarking experiments [10, 41, 71–74]. We estimate the average gate

Table 2. Examples of remote cross-resonance gates with a high concurrence: target cable length, qubit frequency detunings (δ_A, δ_B , and Δ), coupling (g), pulse duration (τ), concurrence for the initial qubit state $|\Phi_+^I\rangle$ (\mathcal{C}_+), average gate fidelity ($\bar{\mathcal{F}}$), and concurrence with dissipation for the initial qubit state $|\Phi_+^I\rangle$ (\mathcal{C}'_+).

Cable length (m)	δ_A	δ_B	$\Delta/(2\pi)$ (GHz)	$g/(2\pi)$ (GHz)	τ (ns)	\mathcal{C}_+	$\bar{\mathcal{F}}$	\mathcal{C}'_+
0.25	0.7	0.3	0.3846	0.03	169.3	1.0000	0.9999	0.9999
0.5	1.25	0.75	0.4348	0.03	152.4	0.9998	0.9998	0.9997
	0.35	0.65	0.2174	0.02	147.3	0.9998	0.9998	0.9996
1.0	2.55	1.25	0.4419	0.02	201.9	0.9928	0.9964	0.9859
	2.5	1.2	0.4302	0.01	385.9	0.9964	0.9976	0.9943
	1.55	1.35	0.3372	0.01	400.3	0.9984	0.9989	0.9975

fidelity $\bar{\mathcal{F}}$ by averaging the final state fidelity \mathcal{F}_i with an echoed remote cross-resonance pulse for sixteen initial qubit states $|\Phi_i^I\rangle = \{|0\rangle, |1\rangle, |+\rangle, |-\rangle\} \otimes \{|0\rangle, |1\rangle, |+\rangle, |-\rangle\}$, where $|+\rangle = (|0\rangle + |1\rangle)/\sqrt{2}$ and $|-\rangle = (|0\rangle + i|1\rangle)/\sqrt{2}$. The remote cross-resonance gates summarized in Table 2 are examined for each coaxial cable length. The phase of the cross-resonance pulse and the phase rotation for the final qubit states are optimized to maximize $\bar{\mathcal{F}}$. We obtain $\bar{\mathcal{F}} > 99.9\%$ for 0.25- and 0.5-m cables and $> 99.5\%$ for a 1-m cable, which are also summarized in Table 2.

3. Dissipative-transmission path

We determine the dissipative properties of the transmission path and perform time evolution simulations for remote cross-resonance gates using these dissipative properties.

3.1. Relaxation time

The Q value of the m th cable standing-wave mode Q_m is given as follows:

$$\begin{aligned}
 1/Q_m &= 1/Q_{\text{Cable}} + 1/Q_{\text{Loss}} \\
 Q_{\text{Loss}} &= \frac{\omega_m L}{\cos^2(2\pi l_{\text{CPW}}/\lambda_{\text{CPW}}^m) R},
 \end{aligned} \tag{6}$$

where Q_{Cable} is the cable specific value, which is 1.2×10^6 for a 0.25-m coaxial cable [5], and Q_{Loss} is determined based on the ratio of l_{CPW} and λ_{CPW}^m . Here, l_{CPW} is presented in Table 1 and $\lambda_{\text{CPW}}^m = 2\pi v_{\text{CPW}}/\omega_m$ is the wavelength of the m th mode in the coplanar waveguide, where $v_{\text{CPW}} = 1.157 \times 10^8$ m/s [5] and $\omega_m = m\omega_{\text{FSR}}$. The equivalent inductance L is given by

$$L \approx \frac{1}{2}(2\mathcal{L}_{\text{CPW}}l_{\text{CPW}} + \mathcal{L}_{\text{Cable}}l_{\text{Cable}}), \tag{7}$$

where $\mathcal{L}_{\text{CPW}} = 402$ nH/m and $\mathcal{L}_{\text{Cable}} = 216$ nH/m are the specific inductances of the coplanar wave guide and coaxial cable, respectively [5]. The resistance between the

coplanar waveguide and coaxial cable R is determined to be $0.0749 \text{ n}\Omega$ by reproducing the experimental results [5]. Figure 6 shows the Q value and relaxation time of each standing-wave mode for each cable length. The relaxation time of the m th mode T_m is obtained by $Q_m = \omega_m T_m$.

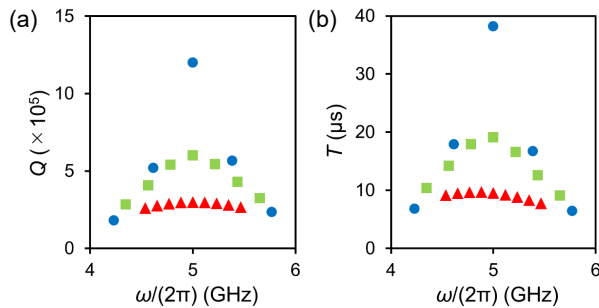


Figure 6. (a) Q value and (b) relaxation time T as functions of the frequency ω of the standing-wave modes of the transmission path. The blue circles, green squares, and red triangles represent the data for 0.25-, 0.5-, and 1-m cables, respectively.

3.2. Time evolution simulation

To reveal the effect of dissipation through the multimode transmission paths, we solve the master equations by including the amplitude damping, with the relaxation time T_m determined in the previous section using the QuTip framework [69, 70]. We consider only the dissipation of the transmission path to isolate the cable dissipation effect; in other words, we do not consider decoherence due to qubits.

We focus on the remote cross-resonance gates presented in Table 2 for each cable length. The concurrence for the initial qubit state of $|\Phi_+^I\rangle$ with dissipation \mathcal{C}'_+ are examined to compare with \mathcal{C}_+ . The obtained \mathcal{C}'_+ are summarized in Table 2. For 0.25- and 0.5-m coaxial cables, \mathcal{C}'_+ is only 0.01%–0.02% less than \mathcal{C}_+ and the dissipation effect is negligible. For the 1-m cable, however, the effect is much larger and \mathcal{C}'_+ is 0.69% less than \mathcal{C}_+ for $g/(2\pi) = 0.02 \text{ GHz}$ and 0.09%–0.21% for $g/(2\pi) = 0.01 \text{ GHz}$. Reducing the coupling g has an advantage despite the increase in pulse duration τ even when cable dissipation is considered.

4. Leakage and single-qubit gate

Finally, we discuss leakage and single-qubit gates in settings for remote cross-resonance. For the leakage, we examine the time evolution of the initial qubit states of $|00\rangle$, $|01\rangle$, $|10\rangle$, and $|11\rangle$ without any driving pulse, i.e., using the H_0 in Eq. (2). In view of the results of remote cross-resonance gates, the coupling is set to $g/(2\pi) = 0.03, 0.02,$ and 0.01 GHz for 0.25-, 0.5-, and 1-m coaxial cables, respectively. The range $0.1 \leq \delta_A \leq 0.9$ and $0.1 \leq \delta_B \leq 0.9$ is examined for each case. When the dissipation is not considered, the occupation probabilities for all initial qubit states remain 100.00% in 200 ns for all cable lengths.

Next, we consider the dissipation of the transmission path. We do not consider the decoherence due to qubits to isolate the cable dissipation effect. Even when the dissipation is considered, the occupation probability of the $|00\rangle$ initial qubit state remains 100.00% for 200 ns. Other results are presented in Appendix C, Figs. C1–C3. For 0.25- and 0.5 m cables, the occupation probabilities for $|01\rangle$ and $|10\rangle$ in the area corresponding to the remote cross-resonance gates in Table 2 are above 99.9%, while those for $|11\rangle$ are less than 99.9%. For a 1-m cable, the occupation probabilities are between 99.5% and 99.9% for all initial qubit states. These results mean that although reducing the coupling leads to considerable fidelities for longer cable lengths, tunable couplers can be useful even when connecting different frequency qubits, as used in previous quantum-state-transfer experiments [5, 6, 25, 26].

For single-qubit gates, we consider a π rotation around the x axis of Q^A . In Eq. (2), $\tilde{\omega}_B$ is replaced by $\tilde{\omega}_A$ and a raised-cosine pulse envelope is used for $\Omega(t)$. The amplitude of the flat part of the signal is set to $\Omega_0 = 0.005\tilde{\omega}_A$ and the raised-cosine duration is set to $\tau_0 = 100 \times 2\pi/\tilde{\omega}_A$. The final state fidelities are averaged for the initial qubit states of $|00\rangle$, $|01\rangle$, $|10\rangle$, and $|11\rangle$. The pulse duration is optimized for the maximum averaged state fidelity for each δ_A and δ_B . For a 0.25-m cable, the range $0.1 \leq \delta_A \leq 0.9$ and $0.1 \leq \delta_B \leq 0.9$ is examined. The results are presented in Fig. 7. We find that the fidelities obtained for $\delta_A = 0.5$ are $\sim 99.8\%$, which are lower than the others of $>99.9\%$. This is also a notable feature of qubits connected through a cable with multimode coupling. When considering the dissipation of the transmission path, we obtain almost the same results, as shown for remote cross-resonance gates in the previous section.

	0.1	0.2	0.3	0.4	0.5	0.6	0.7	0.8	0.9
0.1		0.9995	0.9997	0.9997	0.9997	0.9997	0.9997	0.9997	0.9997
0.2	0.9998		0.9998	0.9998	0.9997	0.9997	0.9999	0.9998	0.9998
0.3	0.9998	0.9998		0.9997	0.9998	0.9997	0.9998	0.9998	0.9998
0.4	0.9996	0.9997	0.9998		0.9997	0.9997	0.9998	0.9998	0.9998
0.5	0.9985	0.9980	0.9978	0.9977		0.9977	0.9977	0.9976	0.9977
0.6	0.9997	0.9997	0.9998	0.9997	0.9998		0.9998	0.9997	0.9997
0.7	0.9997	0.9997	0.9997	0.9998	0.9997	0.9997		0.9997	0.9998
0.8	0.9997	0.9997	0.9997	0.9997	0.9997	0.9997	0.9998		0.9998
0.9	0.9997	0.9997	0.9997	0.9997	0.9996	0.9997	0.9996	0.9997	

Figure 7. Average gate fidelity of π rotations around the x axis of Q^A without dissipation for a 0.25-m coaxial cable. The cells are colored according to their fidelity values. Other explanations are the same as those in Fig. 3.

For 0.5- and 1.0-m cables, we investigate one parameter set for each length of the remote cross-resonance gates listed in Table 2. The case of $\delta_A = 0.35$, $\delta_B = 0.65$, and $g/(2\pi) = 0.02$ GHz for a 0.5-m cable gives average fidelities of 99.99% and 99.97% without and with dissipation, respectively. For a 1-m cable, we examine the case of $\delta_A = 1.55$, $\delta_B = 1.35$, and $g/(2\pi) = 0.01$ GHz. We find that average fidelities without and with dissipation only go up to 99.19% and 99.18%, respectively. In case of a 1-m cable with a narrower mode space, it seems difficult to avoid increasing the occupation probability of states near the energies of $\tilde{\omega}_A, 2\tilde{\omega}_A, 3\tilde{\omega}_A, \dots$, which comprise the cable modes or their hybridized states with qubit excited states. This means that the use of

tunable couplers is increasingly needed.

5. Conclusion

We have proposed remote cross-resonance gates to realize high-precision quantum state transfer and remote entanglement between superconducting fixed-frequency qubits. The Hamiltonian for two qubits connected through a multimode cable has been constructed, and time evolution simulations have been performed. For a 0.25-m cable, there are qubit frequencies to exhibit the concurrence in remote entanglement generation $\mathcal{C}_+ > 99.9\%$ by calibrating the signal frequency and pulse duration, even with ± 38 -MHz qubit frequency error due to manufacturing. A 0.5-m cable also allows manufacturing errors of ± 10 MHz for $\mathcal{C}_+ > 99.9\%$. We have also found that the average gate fidelity, which is a more general characteristic of two-qubit gates, is higher than 99.9%. These high-precision quantum interconnects are promising not only for scaling up quantum computer systems but also for nonlocal connections on a chip and may open new avenues such as non-2D quantum error-correcting codes.

For a 1-m cable with a narrower mode spacing, remote cross-resonance gates with $\mathcal{C}_+ > 99.5\%$ can be achieved by reducing the coupling between the qubits and cable. This is in sharp contrast to quantum state transfer, where a small qubit frequency detuning of 5 MHz notably decreases the efficiency. Although the leakage shows considerable fidelities, it seems difficult to avoid reduction in the fidelity for single-qubit gates on qubits connected a 1-m cable.

The proposed remote cross-resonance gates should first be experimentally tested. In this context, we must introduce the accuracy improvement methods already implemented in single-qubit gates and cross-resonance gates within chips. It is also necessary to seriously consider utilization of tunable couplers between qubits and a coaxial cable even with frequency detunings between the cable mode and the qubits.

Acknowledgments

We would like to thank members of the Quantum Hardware project in Quantum Laboratory for their daily knowledge sharing and discussions.

Appendix A. Quantum state transfer between frequency-detuned qubits

We show the effect of a qubit frequency detuning Δ on quantum state transfer via the standing-wave modes of a cable. Two qubits Q^A and Q^B are connected using a 1-m cable through tunable couplers. Time evolution simulations are performed for the H_0 in Eq. (2) with $M = 43$, $M_{\text{Min}} = 41$, $M_{\text{Max}} = 45$, $\omega_{\text{FSR}}/(2\pi) = 0.1163$ GHz, and $g_A/(2\pi) = g_B/(2\pi) = 0.003$ GHz. After preparing the excited state $|1\rangle$ for Q^A , the tunable couplers are turned on until the occupation probability of state $|1\rangle$, $P_{|1\rangle}$ of Q^B reaches its maximum. The time evolution of $P_{|1\rangle}$ for each qubit and the M th cable mode is depicted in Fig. A1. The final $P_{|1\rangle}$ of Q^B corresponds to the transfer efficiency. The qubit frequency detunings are set to $\Delta_A/(2\pi) = \Delta/(4\pi) + (2 \text{ MHz})$ and $\Delta_B/(2\pi) = -\Delta/(4\pi) + (2 \text{ MHz})$ for the maximum transfer efficiency. We find that a small detuning of $\Delta/(2\pi) = 5$ MHz considerably reduces the efficiency of quantum state transfer.

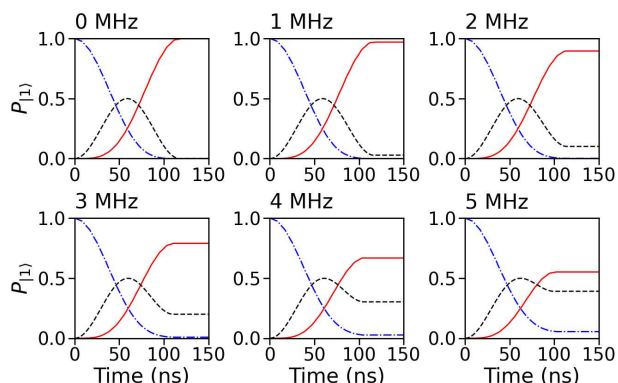


Figure A1. Time evolution of quantum state transfer between frequency-detuned qubits. The qubit frequency detuning of $\Delta/(2\pi)$ is given on the top of each panel. The blue dashed-dotted, red solid, and black dashed curves represent the occupation probabilities of state $|1\rangle$, $P_{|1\rangle}$ for Q^A , Q^B , and the M th cable mode, respectively.

Appendix B. Qubit frequency dependence of remote cross-resonance gates

The primary results for qubit frequency dependence of remote cross-resonance gates are presented in the main text. Here are some additional results. Figure B1(a) shows the results of $g/(2\pi) = 0.02$ GHz for a 0.25-m cable. We cannot find 3×3 cells with $\mathcal{C}_+ > 99.9\%$ as shown in Fig. 3. Figure B1(b) shows the results of $g/(2\pi) = 0.03$ GHz for a 0.5-m cable. We find six 2×2 cells with $\mathcal{C}_+ > 99.9\%$. Figure B1(c) presents the results of $g/(2\pi) = 0.02$ GHz for a 1-m cable. We find 2×2 cells with $\mathcal{C}_+ > 99\%$.

(a)

	0.1	0.2	0.3	0.4	0.5	0.6	0.7	0.8	0.9
0.1	0.9665 72.7	0.9775 111.4	0.9995 159.8	0.9531 219.2	0.9732 254.2	0.9951 269.6	0.9977 273.5	0.9990 244.5	0.9984 187.1
0.2	0.9807 85.6	0.9994 130.1	0.9998 182.7	0.9973 233.3	0.9850 275.4	1.0000 299.8	1.0000 294.6	1.0000 256.4	0.9895 190.5
0.3	0.9905 97.7	0.9993 147.2	0.9979 207.3	0.9997 261.7	0.9914 304.6	0.9999 326.7	1.0000 316.6	0.9999 273.0	0.9998 200.4
0.4	0.9981 109.0	0.9995 165.1	0.9997 229.4	0.9992 290.6	0.9940 334.1	1.0000 355.2	0.9999 340.7	0.9942 290.9	0.9997 212.0
0.5	0.9984 119.9	0.9980 184.6	0.9999 254.0	0.9999 319.5	0.9970 367.4	0.9995 385.0	0.9998 366.9	0.9999 310.1	0.9998 224.4
0.6	0.9975 132.5	0.9989 203.3	0.9996 279.8	0.9997 349.3	0.9979 398.2	0.9964 421.4	0.9991 394.8	1.0000 332.3	0.9999 237.3
0.7	0.9907 145.8	0.9998 224.5	0.9997 308.1	0.9998 384.8	0.9987 436.5	0.9998 453.3	0.9815 426.0	0.9996 356.1	0.9998 253.2
0.8	0.9982 162.3	0.9995 252.5	0.9997 347.8	0.9995 432.2	0.9986 491.8	0.9979 507.4	0.9998 475.1	0.9995 391.0	0.9999 274.6
0.9	0.9916 204.3	0.9947 330.2	0.9980 457.2	0.9960 546.2	0.9971 617.4	0.9991 647.9	0.9983 597.2	0.9978 483.9	0.6168 298.2

(b)

	1.1	1.2	1.3	1.4	1.5	1.6	1.7	1.8	1.9
0.1			0.9660 153.4	0.9815 177.9	0.9800 192.3	0.9967 194.8	0.9991 183.9		
0.2			0.4355 119.0	0.9525 162.1	0.9771 176.0	0.9993 177.1	0.9998 168.3	0.9997 152.5	
0.3	0.9976 105.5	0.9953 125.3	0.6318 162.3	0.7448 184.3	0.9640 172.1	0.9992 172.0	0.9998 163.2	0.9999 148.2	0.9999 130.8
0.4	0.9972 106.8	0.9817 125.3	0.9798 142.3	0.7023 185.1	0.8354 179.9	0.9935 174.1	0.9992 163.6	0.9998 148.6	0.9999 131.3
0.5	0.9944 109.3	0.9972 128.3	0.9978 147.9	0.9754 165.9	0.7234 196.6	0.9438 186.2	0.9944 168.3	0.9994 151.6	0.9998 133.9
0.6	0.9936 113.5	0.9990 133.8	0.9995 155.1	0.9978 173.6	0.9776 186.7	0.6128 190.5	0.9566 181.3	0.9916 157.3	0.9986 138.6
0.7	0.9993 121.1	0.9999 142.7	0.9994 165.3	0.9997 184.3	0.9955 195.3	0.9713 197.8	0.5382 150.2	0.9325 173.3	
0.8		0.9995 157.1	0.9984 182.3	0.9997 203.9	0.9970 215.0	0.9927 218.0	0.9750 199.4	0.5095 142.5	
0.9			0.9980 216.3	0.9977 239.3	0.9967 254.4	0.9996 255.4	0.9952 237.4		

(c)

	2.1	2.2	2.3	2.4	2.5	2.6	2.7	2.8	2.9
1.1									
1.2			0.4283 150.3	0.9566 242.2	0.9559 243.5	0.9860 224.4	0.9957 215.9		
1.3		0.9929 184.3	0.8527 226.5	0.4525 159.9	0.9526 230.4	0.9761 226.5	0.9945 209.1		
1.4		0.9844 185.9	0.9777 201.1	0.8567 243.5	0.4767 168.3	0.9899 228.7	0.9787 210.8	0.9956 192.3	
1.5		0.9942 188.5	0.9955 210.8	0.9642 224.4	0.8787 258.0	0.5032 173.7	0.9835 221.4	0.9870 194.5	
1.6		0.9930 199.5	0.9946 222.3	0.9918 233.3	0.9547 237.2	0.7733 268.7	0.6858 593.9	0.9503 214.5	
1.7		0.9897 215.9	0.9965 241.3	0.9899 254.1	0.9900 702.5	0.9696 249.1	0.5293 239.3		
1.8				0.9858 803.4	0.9837 810.9	0.9668 802.7			
1.9									

Figure B1. Time revolution simulation results of an echoed cross-resonance pulse with the initial qubit state of $|\Phi_+^1\rangle = (|00\rangle + |10\rangle)/\sqrt{2}$ for a coaxial cable. The cable length and coupling $g/(2\pi)$ are (a) 0.25 m and 0.02 GHz, (b) 0.5 m and 0.03 GHz, and (c) 1 m and 0.02 GHz. Other explanations are the same as those in Fig. 3.

Appendix C. Leakage properties

We examine the time evolution of the initial states of $|00\rangle$, $|01\rangle$, $|10\rangle$, and $|11\rangle$ for 200 ns without any driving pulse, i.e., using the H_0 in Eq. (2) for the leakage properties. The coupling is set to $g/(2\pi) = 0.03, 0.02$, and 0.01 GHz for 0.25-, 0.5-, and 1-m coaxial cables, respectively. The range $0.1 \leq \delta_A \leq 0.9$ and $0.1 \leq \delta_B \leq 0.9$ are examined for each case. We present the results for the initial states of $|01\rangle$, $|10\rangle$, and $|11\rangle$ with cable dissipation in Figs. C1–C3 because the occupation probabilities without dissipation for all initial qubit states and those with dissipation for the $|00\rangle$ initial qubit state remain 100.00% for 200 ns. For 0.25- and 0.5 m cables, the occupation probabilities for $|01\rangle$ and $|10\rangle$ in the area corresponding to the remote cross-resonance gates in Table 2 are above 99.9%, while those for $|11\rangle$ are less than 99.9%. For a 1-m cable, the occupation probabilities are between 99.5% and 99.9% for all initial qubit states. These results mean that reducing the coupling leads to considerable fidelities for longer cable lengths.

	0.1	0.2	0.3	0.4	0.5	0.6	0.7	0.8	0.9
(a)		0.9992	0.9994	0.9995	0.9995	0.9994	0.9992	0.9987	0.9973
0.1		0.9985	0.9992	0.9994	0.9995	0.9995	0.9994	0.9992	0.9987
0.2	0.9985		0.9994	0.9995	0.9995	0.9994	0.9992	0.9987	0.9973
0.3	0.9985	0.9992		0.9995	0.9995	0.9994	0.9992	0.9987	0.9973
0.4	0.9985	0.9992	0.9994		0.9995	0.9994	0.9992	0.9987	0.9973
0.5	0.9985	0.9992	0.9994	0.9995		0.9994	0.9992	0.9987	0.9973
0.6	0.9986	0.9992	0.9994	0.9995	0.9995		0.9992	0.9987	0.9973
0.7	0.9986	0.9992	0.9994	0.9995	0.9995	0.9994		0.9987	0.9973
0.8	0.9986	0.9992	0.9994	0.9995	0.9995	0.9994	0.9992		0.9973
0.9	0.9986	0.9992	0.9994	0.9995	0.9995	0.9994	0.9992	0.9987	

	0.1	0.2	0.3	0.4	0.5	0.6	0.7	0.8	0.9
(b)		0.9984	0.9985	0.9985	0.9985	0.9985	0.9985	0.9985	0.9985
0.1		0.9991	0.9991	0.9992	0.9992	0.9992	0.9992	0.9992	0.9992
0.2	0.9991		0.9994	0.9994	0.9994	0.9994	0.9994	0.9994	0.9994
0.3	0.9994	0.9994		0.9994	0.9994	0.9994	0.9994	0.9994	0.9994
0.4	0.9995	0.9995	0.9995		0.9995	0.9995	0.9995	0.9995	0.9995
0.5	0.9994	0.9994	0.9994	0.9994		0.9994	0.9994	0.9994	0.9994
0.6	0.9993	0.9993	0.9993	0.9993	0.9993		0.9993	0.9993	0.9993
0.7	0.9991	0.9991	0.9991	0.9991	0.9991	0.9991		0.9991	0.9991
0.8	0.9985	0.9985	0.9985	0.9985	0.9985	0.9985	0.9984		0.9984
0.9	0.9970	0.9970	0.9970	0.9970	0.9970	0.9970	0.9970	0.9970	

	0.1	0.2	0.3	0.4	0.5	0.6	0.7	0.8	0.9
(c)		0.9976	0.9979	0.9980	0.9980	0.9979	0.9977	0.9972	0.9958
0.1		0.9976	0.9983	0.9986	0.9987	0.9986	0.9984	0.9979	0.9965
0.2	0.9976		0.9986	0.9988	0.9989	0.9988	0.9986	0.9981	0.9967
0.3	0.9979	0.9986		0.9989	0.9989	0.9988	0.9986	0.9981	0.9967
0.4	0.9980	0.9987	0.9989		0.9990	0.9989	0.9987	0.9982	0.9968
0.5	0.9980	0.9986	0.9989	0.9990		0.9989	0.9986	0.9981	0.9967
0.6	0.9979	0.9985	0.9988	0.9989	0.9988		0.9985	0.9980	0.9966
0.7	0.9976	0.9983	0.9985	0.9986	0.9986	0.9985		0.9977	0.9963
0.8	0.9970	0.9977	0.9979	0.9980	0.9980	0.9979	0.9977		0.9957
0.9	0.9956	0.9962	0.9965	0.9965	0.9965	0.9964	0.9962	0.9956	

Figure C1. Dissipative leakage properties for a 0.25-m coaxial cable with $g/(2\pi) = 0.03$ GHz: probabilities that the initial qubit states of (a) $|01\rangle$, (b) $|10\rangle$, and (c) $|11\rangle$ are retained in 200 ns. Other explanations are the same as those in Fig. 3.

(a)

	0.1	0.2	0.3	0.4	0.5	0.6	0.7	0.8	0.9
0.1		0.9991	0.9994	0.9995	0.9996	0.9995	0.9994	0.9991	0.9983
0.2	0.9983		0.9994	0.9995	0.9996	0.9995	0.9994	0.9991	0.9983
0.3	0.9984	0.9991		0.9996	0.9996	0.9995	0.9994	0.9991	0.9983
0.4	0.9984	0.9991	0.9994		0.9996	0.9995	0.9994	0.9991	0.9983
0.5	0.9984	0.9991	0.9994	0.9996		0.9995	0.9994	0.9991	0.9983
0.6	0.9984	0.9991	0.9994	0.9996	0.9996		0.9994	0.9991	0.9983
0.7	0.9984	0.9991	0.9994	0.9996	0.9996	0.9995		0.9991	0.9983
0.8	0.9984	0.9991	0.9994	0.9996	0.9996	0.9995	0.9994		0.9983
0.9	0.9985	0.9991	0.9994	0.9996	0.9996	0.9995	0.9994	0.9991	

(b)

	0.1	0.2	0.3	0.4	0.5	0.6	0.7	0.8	0.9
0.1		0.9983	0.9983	0.9984	0.9984	0.9984	0.9984	0.9984	0.9984
0.2	0.9990		0.9991	0.9991	0.9991	0.9991	0.9991	0.9991	0.9991
0.3	0.9994	0.9994		0.9994	0.9994	0.9994	0.9994	0.9994	0.9994
0.4	0.9995	0.9995	0.9995		0.9995	0.9995	0.9995	0.9995	0.9995
0.5	0.9996	0.9996	0.9996	0.9996		0.9996	0.9996	0.9996	0.9996
0.6	0.9995	0.9995	0.9995	0.9995	0.9995		0.9995	0.9995	0.9995
0.7	0.9993	0.9993	0.9993	0.9993	0.9993	0.9993		0.9993	0.9993
0.8	0.9990	0.9990	0.9990	0.9990	0.9990	0.9990	0.9990		0.9990
0.9	0.9982	0.9982	0.9981	0.9981	0.9981	0.9981	0.9981	0.9981	

(c)

	0.1	0.2	0.3	0.4	0.5	0.6	0.7	0.8	0.9
0.1		0.9973	0.9977	0.9979	0.9979	0.9979	0.9978	0.9975	0.9967
0.2	0.9973		0.9981	0.9985	0.9986	0.9987	0.9986	0.9985	0.9974
0.3	0.9977	0.9985		0.9988	0.9990	0.9989	0.9988	0.9985	0.9977
0.4	0.9979	0.9986	0.9989		0.9991	0.9991	0.9989	0.9986	0.9978
0.5	0.9979	0.9987	0.9990	0.9991		0.9991	0.9989	0.9986	0.9978
0.6	0.9979	0.9986	0.9989	0.9990	0.9991		0.9989	0.9986	0.9978
0.7	0.9978	0.9985	0.9988	0.9989	0.9989	0.9989		0.9987	0.9976
0.8	0.9974	0.9981	0.9984	0.9985	0.9985	0.9985	0.9984		0.9972
0.9	0.9966	0.9973	0.9976	0.9977	0.9977	0.9977	0.9975	0.9972	

Figure C2. Dissipative leakage properties for a 0.5-m coaxial cable with $g/(2\pi) = 0.02$ GHz: probabilities that the initial qubit states of (a) $|01\rangle$, (b) $|10\rangle$, and (c) $|11\rangle$ are retained in 200 ns. Other explanations are the same as those in Fig. 3.

(a)

	0.1	0.2	0.3	0.4	0.5	0.6	0.7	0.8	0.9
0.1		0.9967	0.9980	0.9985	0.9987	0.9986	0.9981	0.9971	0.9944
0.2	0.9938		0.9968	0.9980	0.9985	0.9987	0.9986	0.9981	0.9970
0.3	0.9939	0.9968		0.9981	0.9985	0.9987	0.9986	0.9981	0.9970
0.4	0.9940	0.9969	0.9981		0.9985	0.9987	0.9986	0.9981	0.9970
0.5	0.9941	0.9969	0.9981	0.9985		0.9987	0.9986	0.9981	0.9970
0.6	0.9941	0.9969	0.9981	0.9985	0.9987		0.9986	0.9981	0.9970
0.7	0.9942	0.9969	0.9981	0.9985	0.9987	0.9986		0.9981	0.9970
0.8	0.9942	0.9970	0.9981	0.9986	0.9987	0.9986	0.9981		0.9970
0.9	0.9942	0.9970	0.9981	0.9986	0.9987	0.9986	0.9981	0.9970	

(b)

	0.1	0.2	0.3	0.4	0.5	0.6	0.7	0.8	0.9
0.1		0.9937	0.9938	0.9939	0.9940	0.9941	0.9941	0.9941	0.9942
0.2	0.9967		0.9968	0.9969	0.9969	0.9969	0.9969	0.9969	0.9969
0.3	0.9980	0.9980		0.9981	0.9981	0.9981	0.9981	0.9981	0.9981
0.4	0.9985	0.9985	0.9985		0.9985	0.9985	0.9985	0.9985	0.9985
0.5	0.9987	0.9987	0.9987	0.9987		0.9987	0.9987	0.9987	0.9987
0.6	0.9986	0.9986	0.9986	0.9986	0.9986		0.9986	0.9986	0.9986
0.7	0.9982	0.9982	0.9981	0.9981	0.9981	0.9981		0.9981	0.9981
0.8	0.9971	0.9971	0.9971	0.9971	0.9971	0.9971	0.9971		0.9970
0.9	0.9946	0.9946	0.9945	0.9945	0.9945	0.9945	0.9945	0.9945	

(c)

	0.1	0.2	0.3	0.4	0.5	0.6	0.7	0.8	0.9
0.1		0.9903	0.9918	0.9924	0.9927	0.9926	0.9922	0.9911	0.9885
0.2	0.9904		0.9935	0.9948	0.9954	0.9955	0.9950	0.9939	0.9913
0.3	0.9919	0.9949		0.9961	0.9966	0.9967	0.9966	0.9951	0.9924
0.4	0.9925	0.9954	0.9966		0.9971	0.9972	0.9971	0.9956	0.9929
0.5	0.9927	0.9956	0.9967	0.9972		0.9974	0.9972	0.9958	0.9930
0.6	0.9927	0.9955	0.9966	0.9971	0.9972		0.9971	0.9956	0.9929
0.7	0.9923	0.9951	0.9962	0.9967	0.9968	0.9967		0.9951	0.9924
0.8	0.9913	0.9940	0.9952	0.9956	0.9958	0.9956	0.9952		0.9913
0.9	0.9888	0.9915	0.9926	0.9931	0.9932	0.9931	0.9926	0.9915	

Figure C3. Dissipative leakage properties for a 1-m coaxial cable with $g/(2\pi) = 0.01$ GHz: probabilities that the initial qubit states of (a) $|01\rangle$, (b) $|10\rangle$, and (c) $|11\rangle$ are retained in 200 ns. Other explanations are the same as those in Fig. 3.

- [1] Byrd G T and Ding Y 2023 *Computer* **56** 20–29
- [2] Bravyi S, Dial O, Gambetta J M, Gil D and Nazario Z 2022 *J. Appl. Phys.* **132** 160902
- [3] Awschalom D, Berggren K K, Bernien H, Bhave S, Carr L D, Davids P, Economou S E, Englund D, Faraon A, Fejer M, Guha S, Gustafsson M V, Hu E, Jiang L, Kim J, Korzh B, Kumar P, Kwiat P G, Lončar M, Lukin M D, Miller D A, Monroe C, Nam S W, Narang P, Orcutt J S, Raymer M G, Safavi-Naeini A H, Spiropulu M, Srinivasan K, Sun S, Vučković J, Waks E, Walsworth R, Weiner A M and Zhang Z 2021 *PRX Quantum* **2**(1) 017002
- [4] Gold A, Paquette J P, Stockklauser A, Reagor M J, Alam M S, Bestwick A, Didier N, Nersisyan A, Oruc F, Razavi A, Scharmann B, Sete E A, Sur B, Venturelli D, Winkleblack C J, Wudarski F, Harburn M and Rigetti C 2021 *npj Quantum Inf.* **7** 142
- [5] Niu J, Zhang L, Liu Y, Qiu J, Huang W, Huang J, Jia H, Liu J, Tao Z, Wei W, Zhou Y, Zou W, Chen Y, Deng X, Deng X, Hu C, Hu L, Li J, Tan D, Xu Y, Yan F, Yan T, Liu S, Zhong Y, Cleland A N and Yu D 2023 *Nat. Electron.* **6** 235–241
- [6] Zhong Y, Chang H S, Bienfait A, Dumur É, Chou M H, Conner C R, Grebel J, Povey R G, Yan H, Schuster D I and Cleland A N 2021 *Nature* **590** 571–575
- [7] Mirhosseini M, Sipahigil A, Kalae M and Painter O 2020 *Nature* **588** 599–603
- [8] Conner C R, Bienfait A, Chang H S, Chou M H, Dumur É, Grebel J, Peairs G A, Povey R G, Yan H, Zhong Y P and Cleland A N 2021 *Appl. Phys. Lett.* **118** 232602
- [9] Kosen S, Li H X, Rommel M, Shiri D, Warren C, Grönberg L, Salonen J, Abad T, Biznárová J, Caputo M, Chen L, Grigoras K, Johansson G, Kockum A F, Križan C, Lozano D P, Norris G J, Osman A, Fernández-Pendás J, Ronzani A, Roudsari A F, Simbierowicz S, Tancredi G, Wallraff A, Eichler C, Govenius J and Bylander J 2022 *Quantum Sci. Technol.* **7** 035018
- [10] Marxer F, Vepsäläinen A, Jolin S W, Tuorila J, Landra A, Ockeloen-Korppi C, Liu W, Ahonen O, Auer A, Belzane L, Bergholm V, Chan C F, Chan K W, Hiltunen T, Hotari J, Hyypä E, Ikonen J, Janzso D, Koistinen M, Kotilahti J, Li T, Luus J, Papic M, Partanen M, Rabinä J, Rosti J, Savvitskyi M, Seppälä M, Sevriuk V, Takala E, Tarasinski B, Thapa M J, Tosto F, Vorobeve N, Yu L, Tan K Y, Hassel J, Möttönen M and Heinsoo J 2023 *PRX Quantum* **4**(1) 010314
- [11] Campbell E T, Terhal B M and Vuillot C 2017 *Nature* **549** 172–179
- [12] Bravyi S B and Kitaev A Y 1998 *quant-ph/9811052*
- [13] Dennis E, Kitaev A, Landahl A and Preskill J 2002 *J. Math. Phys.* **43** 4452–4505
- [14] Kitaev A Y 2003 *Ann. Phys.* **303** 2–30
- [15] Raussendorf R and Harrington J 2007 *Phys. Rev. Lett.* **98**(19) 190504
- [16] Fowler A G, Mariantoni M, Martinis J M and Cleland A N 2012 *Phys. Rev. A* **86**(3) 032324
- [17] Horsman D, Fowler A G, Devitt S and Van Meter R 2012 *New J. Phys.* **14**(3) 123011
- [18] Zhao Y, Ye Y, Huang H L, Zhang Y, Wu D, Guan H, Zhu Q, Wei Z, He T, Cao S, Chen F, Chung T H, Deng H, Fan D, Gong M, Guo C, Guo S, Han L, Li N, Li S, Li Y, Liang F, Lin J, Qian H, Rong H, Su H, Sun L, Wang S, Wu Y, Xu Y, Ying C, Yu J, Zha C, Zhang K, Huo Y H, Lu C Y, Peng C Z, Zhu X and Pan J W 2022 *Phys. Rev. Lett.* **129**(3) 030501
- [19] Krinner S, Lacroix N, Remm A, Paolo A D, Genois E, Leroux C, Hellings C, Lazar S, Swiadek F, Herrmann J, Norris G J, Andersen C K, Müller M, Blais A, Eichler C and Wallraff A 2022 *Nature* **605** 669
- [20] Google Quantum AI 2023 *Nature* **614** 676–681
- [21] Cirac J I, Zoller P, Kimble H J and Mabuchi H 1997 *Phys. Rev. Lett.* **78**(16) 3221–3224
- [22] Kurpiers P, Magnard P, Walter T, Royer B, Pechal M, Heinsoo J, Salathé Y, Akin A, Storz S, Besse J C, Gasparinetti S, Blais A and Wallraff A 2018 *Nature* **558** 264–267
- [23] Axline C J, Burkhardt L D, Pfaff W, Zhang M, Chou K, Campagne-Ibarcq P, Reinhold P, Frunzio L, Girvin S M, Jiang L, Devoret M H and Schoelkopf R J 2018 *Nature Phys.* **14** 705–710
- [24] Campagne-Ibarcq P, Zalys-Geller E, Narla A, Shankar S, Reinhold P, Burkhardt L, Axline C, Pfaff W, Frunzio L, Schoelkopf R J and Devoret M H 2018 *Phys. Rev. Lett.* **120**(20) 200501
- [25] Leung N, Lu Y, Chakram S, Naik R K, Earnest N, Ma R, Jacobs K, Cleland A N and Schuster D I 2019 *npj Quantum Inf.* **5** 18

- [26] Zhong Y P, Chang H S, Satzinger K J, Chou M H, Bienfait A, Conner C R, Dumur É, Grebel J, Peairs G A, Povey R G, Schuster D I and Cleland A N 2019 *Nature Phys.* **15** 741–744
- [27] Magnard P, Storz S, Kurpiers P, Schär J, Marxer F, Lütolf J, Walter T, Besse J C, Gabureac M, Reuer K, Akin A, Royer B, Blais A and Wallraff A 2020 *Phys. Rev. Lett.* **125**(26) 260502
- [28] Chang H S, Zhong Y P, Bienfait A, Chou M H, Conner C R, Dumur E, Grebel J, Peairs G A, Povey R G, Satzinger K J and Cleland A N 2020 *Phys. Rev. Lett.* **124**(24) 240502
- [29] Burkhardt L D, Teoh J D, Zhang Y, Axline C J, Frunzio L, Devoret M, Jiang L, Girvin S and Schoelkopf R 2021 *PRX Quantum* **2**(3) 030321
- [30] Pechal M and Safavi-Naeini A H 2017 *Phys. Rev. A* **96**(4) 042305
- [31] Safavi-Naeini A H, Thourhout D V, Baets R and Laer R V 2019 *Optica* **6** 213–232
- [32] Dumur É, Satzinger K J, Peairs G A, Chou M H, Bienfait A, Chang H S, Conner C R, Grebel J, Povey R G, Zhong Y P and Cleland A N 2021 *npj Quantum Inf.* **7** 173
- [33] Han X, Fu W, Zou C L, Jiang L and Tang H X 2021 *Optica* **8** 1050–1064
- [34] Andrews R W, Peterson R W, Purdy T P, Cicak K and Simmonds R W, Regal C A and Lehnert K W 2014 *Nature Phys.* **10** 321–326
- [35] Williamson L A, Chen Y H and Longdell J J 2014 *Phys. Rev. Lett.* **113**(20) 203601
- [36] Hisatomi R, Osada A, Tabuchi Y, Ishikawa T, Noguchi A, Yamazaki R, Usami K and Nakamura Y 2016 *Phys. Rev. B* **93**(17) 174427
- [37] Krastanov S, Raniwala H, Holzgrafe J, Jacobs K, Lončar M, Reagor M J and Englund D R 2021 *Phys. Rev. Lett.* **127**(4) 040503
- [38] Tu H T, Liao K Y, Zhang Z X, Liu X H, Zheng S Y, Yang S Z, Zhang X D, Yan H and Zhu S L 2022 *Nat. Photon.* **16** 291–296
- [39] Hönl S, Popoff Y, Caimi D, Beccari A, Kippenberg T J and Seidler P 2022 *Nat. Commun.* **13** 2065
- [40] Chiappina P, Banker J, Meesala S, Lake D, Wood S and Painter O 2023 *Opt. Express* **31** 22914–22927
- [41] Barends R, Kelly J, Megrant A, Veitia A, Sank D, Jeffrey E, White T C, Mutus J, Fowler A G, Campbell B, Chen Y, Chen Z, Chiaro B, Dunsworth A, Neill C, O’Malley P, Roushan P, Vainsencher A, Wenner J, Korotkov A N, Cleland A N and Martinis J M 2014 *Nature* **508** 500–503
- [42] DiCarlo L, Chow J M, Gambetta J M, Bishop L S, Johnson B R, Schuster D I, Majer J, Blais A, Frunzio L, Girvin S M and Schoelkopf R J 2009 *Nature* **460** 240–244
- [43] Kelly J, Barends R, Fowler A G, Megrant A, Jeffrey E, White T C, Sank D, Mutus J Y, Campbell B, Chen Y, Chen Z, Chiaro B, Dunsworth A, Hoi I C, Neill C, O’Malley P J J, Quintana C, Roushan P, Vainsencher A, Wenner J, Cleland A N and Martinis J M 2015 *Nature* **519** 66–69
- [44] Reagor M, Osborn C B, Tezak N, Staley A, Prawiroatmodjo G, Scheer M, Alidoust N, Sete E A, Didier N, da Silva M P, Acala E, Angeles J, Bestwick A, Block M, Bloom B, Bradley A, Bui C, Caldwell S, Capelluto L, Chilcott R, Cordova J, Crossman G, Curtis M, Deshpande S, Bouayadi T E, Girshovich D, Hong S, Hudson A, Karalekas P, Kuang K, Lenihan M, Manenti R, Manning T, Marshall J, Mohan Y, O’Brien W, Otterbach J, Papageorge A, Paquette J P, Pelstring M, Polloreno A, Rawat V, Ryan C A, Renzas R, Rubin N, Russel D, Rust M, Scarabelli D, Selvanayagam M, Sinclair R, Smith R, Suska M, To T W, Vahidpour M, Vodrahalli N, Whyland T, Yadav K, Zeng W and Rigetti C T 2018 *Sci. Adv.* **4** eaao3603
- [45] Chen Y, Neill C, Roushan P, Leung N, Fang M, Barends R, Kelly J, Campbell B, Chen Z, Chiaro B, Dunsworth A, Jeffrey E, Megrant A, Mutus J Y, O’Malley P J J, Quintana C M, Sank D, Vainsencher A, Wenner J, White T C, Geller M R, Cleland A N and Martinis J M 2014 *Phys. Rev. Lett.* **113**(22) 220502
- [46] Koch J, Yu T M, Gambetta J, Houck A A, Schuster D I, Majer J, Blais A, Devoret M H, Girvin S M and Schoelkopf R J 2007 *Phys. Rev. A* **76**(4) 042319
- [47] Allman M S, Whittaker J D, Castellanos-Beltran M, Cicak K, da Silva F, DeFeo M P, Lecocq F, Sirois A, Teufel J D, Aumentado J and Simmonds R W 2014 *Phys. Rev. Lett.* **112**(12) 123601
- [48] Sirois A J, Castellanos-Beltran M A, DeFeo M P, Ranzani L, Lecocq F, Simmonds R W, Teufel

- J D and Aumentado J 2015 *Appl. Phys. Lett.* **106** 172603
- [49] Axline C, Reagor M, Heeres R, Reinhold P, Wang C, Shain K, Pfaff W, Chu Y, Frunzio L and Schoelkopf R J 2016 *Appl. Phys. Lett.* **109** 042601
- [50] Reagor M, Pfaff W, Axline C, Heeres R W, Ofek N, Sliwa K, Holland E, Wang C, Blumoff J, Chou K, Hatridge M J, Frunzio L, Devoret M H, Jiang L and Schoelkopf R J 2016 *Phys. Rev. B* **94**(1) 014506
- [51] McKay D C, Filipp S, Mezzacapo A, Magesan E, Chow J M and Gambetta J M 2016 *Phys. Rev. Appl.* **6**(6) 064007
- [52] Lu Y, Chakram S, Leung N, Earnest N, Naik R K, Huang Z, Groszkowski P, Kapit E, Koch J and Schuster D I 2017 *Phys. Rev. Lett.* **119**(15) 150502
- [53] Jurcevic P, Javadi-Abhari A, Bishop L S, Lauer I, Bogorin D F, Brink M, Capelluto L, G?nl?k O, Itoko T, Kanazawa N, Kandala A, Keefe G A, Krsulich K, Landers W, Lewandowski E P, McClure D T, Nannicini G, Narasgond A, Nayfeh H M, Pritchett E, Rothwell M B, Srinivasan S, Sundaresan N, Wang C, Wei K X, Wood C J, Yau J B, Zhang E J, Dial O E, Chow J M and Gambetta J M 2021 *Quantum Sci. Technol.* **6** 025020
- [54] Place A P M, Rodgers L V H, Mundada P, Smitham B M, Fitzpatrick M, Leng Z, Premkumar A, Bryon J, Vrajitoarea A, Sussman S, Cheng G, Madhavan T, Babla H K, Le X H, Gang Y, Jäck B, Gyenis A, Yao N, Cava R J, de Leon N P and Houck A A 2021 *Nat. Commun.* **12** 1779
- [55] Hertzberg J B, Zhang E J, Rosenblatt S, Magesan E, Smolin J A, Yau J B, Adiga V P, Sandberg M, Brink M, Chow J M and Orcut J S 2021 *npj Quantum Inf.* **7** 129
- [56] Zhang E J, Srinivasan S, Sundaresan N, Bogorin D F, Martin Y, Hertzberg J B, Timmerwilke J, Pritchett E J, Yau J B, Wang C, Landers W, Lewandowski E P, Narasgond A, Rosenblatt S, Keefe G A, Lauer I, Rothwell M B, McClure D T, Dial O E, Orcutt J S, Brink M and Chow J M 2022 *Sci. Adv.* **8** eabi6690
- [57] Rigetti C and Devoret M 2010 *Phys. Rev. B* **81**(13) 134507
- [58] Chow J M, Córcoles A D, Gambetta J M, Rigetti C, Johnson B R, Smolin J A, Rozen J R, Keefe G A, Rothwell M B, Ketchen M B and Steffen M 2011 *Phys. Rev. Lett.* **107**(8) 080502
- [59] Córcoles A D, Gambetta J M, Chow J M, Smolin J A, Ware M, Strand J, Plourde B L T and Steffen M 2013 *Phys. Rev. A* **87**(3) 030301
- [60] Sheldon S, Magesan E, Chow J M and Gambetta J M 2016 *Phys. Rev. A* **93**(6) 060302
- [61] Patterson A, Rahamim J, Tsunoda T, Spring P, Jebari S, Ratter K, Mergenthaler M, Tancredi G, Vlastakis B, Esposito M and Leek P 2019 *Phys. Rev. Appl.* **12**(6) 064013
- [62] Sundaresan N, Lauer I, Pritchett E, Magesan E, Jurcevic P and Gambetta J M 2020 *PRX Quantum* **1**(2) 020318
- [63] Kandala A, Wei K X, Srinivasan S, Magesan E, Carnevale S, Keefe G A, Klaus D, Dial O and McKay D C 2021 *Phys. Rev. Lett.* **127**(13) 130501
- [64] Heya K and Kanazawa N 2021 *PRX Quantum* **2**(4) 040336
- [65] Malekakhlagh M and Magesan E 2022 *Phys. Rev. A* **105**(1) 012602
- [66] Sundaresan N M, Liu Y, Sadri D, Szöcs L J, Underwood D L, Malekakhlagh M, Türeci H E and Houck A A 2015 *Phys. Rev. X* **5**(2) 021035
- [67] Motzoi F, Gambetta J M, Reberstrost P and Wilhelm F K 2009 *Phys. Rev. Lett.* **103**(11) 110501
- [68] Gambetta J M, Motzoi F, Merkel S T and Wilhelm F K 2011 *Phys. Rev. A* **83**(1) 012308
- [69] Johansson J, Nation P and Nori F 2012 *Comp. Phys. Comm.* **183** 1760–1772
- [70] Johansson J, Nation P and Nori F 2013 *Comp. Phys. Comm.* **184** 1234
- [71] Magesan E, Gambetta J M and Emerson J 2011 *Phys. Rev. Lett.* **106**(18) 180504
- [72] Magesan E, Gambetta J M, Johnson B R, Ryan C A, Chow J M, Merkel S T, da Silva M P, Keefe G A, Rothwell M B, Ohki T A, Ketchen M B and Steffen M 2012 *Phys. Rev. Lett.* **109**(8) 080505
- [73] Sheldon S, Bishop L S, Magesan E, Filipp S, Chow J M and Gambetta J M 2016 *Phys. Rev. A* **93**(1) 012301
- [74] Harper R and Flammia S T 2017 *Quantum Sci. Technol.* **2** 015008